Supplementary information for near-unity broadband omnidirectional emissivity via femtosecond laser surface processing

Andrew Reicks[1,*], Alfred Tsubaki[1], Mark Anderson[2], Jace Wieseler[2], Larousse Khosravi Khorashad[1], Jeffrey E. Shield[2], George Gogos[2], Dennis Alexander[1], Christos Argyropoulos[1,*,+], and Craig Zuhlke[1,*,+]

[1] Department of Electrical & Computer Engineering, University of Nebraska-Lincoln, 1400 R St. Lincoln, Nebraska 68588, USA

[2] Department of Mechanical & Materials Engineering, University of Nebraska-Lincoln, 1400 R St. Lincoln, Nebraska 68588, USA

*Correspondence and requests for materials should be addressed to Andrew Reicks, areicks2@unl.edu, Christos Argyropoulos, christos.argyropoulos@unl.edu, and Craig Zuhlke, czuhlke@unl.edu

[+]These authors jointly supervised this work.

Supplementary Discussion 1

Emissivity of metals and dielectrics. Emissivity is the dimensionless ratio used to describe how efficiently an absorbing surface emits thermal energy, where zero represents a perfect reflector and one represents a perfect emitter. The spectral directional emissivity, $\varepsilon(\lambda, \theta, \varphi, T)$, describes the emissivity of a surface at a particular wavelength, orientation and temperature. The spectral hemispherical emissivity, $\varepsilon(\lambda,T)$, is computed by integrating the spectral directional emissivity over all emission angles at a particular fixed wavelength and temperature. Lastly, the total hemispherical emissivity, $\varepsilon(T)$, is computed by integrating the spectral directional emissivity over all emission directions and in the wavelength range of interest but for a fixed temperature.

Polished metals usually have a low hemispherical emissivity with a higher directional emissivity at low angles relative to the surface normal. When roughness or oxidation is taken into account, the emissivity is usually increased. Generally, the increase of surface roughness leads to an increase in emissivity independent of the wavelength[1,2]. The increase in emissivity caused by roughness is typically illustrated by the optical roughness metric, i.e., the ratio of wavelength divided by the surface roughness. If this ratio is small (less than 0.2), the surface can be described as optically smooth and its properties approach that of an ideal smooth surface with emissivity computed by theory using Maxwell's equations. If this ratio is large, then a geometric optics approach or full-wave electromagnetic simulations must be utilized to take into account the surface morphology[3]. Emissivity is also a function of the surface temperature, wavelength, and observation angle. The effect of these properties can vary greatly depending on the material.

In metals the effect of temperature on emissivity is primarily dependent on the temperature dependent resistivity of the material. The Hagen-Rubens relation shows that for most materials the emissivity is proportional to the square root of resistivity, for sufficiently short wavelengths[2]. Specifically, for aluminum, experimental data has shown that over the temperature range of 0 ^{o}C to 400 ^{o}C the resistivity can be approximated by a linear equation. The resulting effect on emissivity is weak and causes a

variance of approximately 0.006 to 0.008 per hundred degrees Celsius[4–6]. Since this value is so small over such a wide temperature range, the effect of temperature on emissivity is ignored here. For wavelengths longer than 1 μm the directional emissivity of metals tends to increase at large angles, leading to a "flat top" profile (an example of this effect is demonstrated in Supplementary Fig. S2).

For dielectric materials like metal oxides, temperature typically has even less effect on emissivity than for metals. The spectral properties of dielectrics change very slowly with temperature since the refractive index is not a strong function of temperature. For dielectrics, the most significant effect of temperature is related to measuring their thermal radiation power because the wavelength shift in the blackbody radiation distribution needs to be considered[2]. The spectral range considered for this paper corresponds to the atmospheric window from 7.5 to 14 μm or peak blackbody radiation from -66 ºC to 110 ºC. Unlike metals, in dielectrics the directional emissivity tends to decrease at large angles. However, this can vary greatly with surface roughness.

The FLSP surfaces are a combination of dielectric and metal materials and both must be considered for understanding the increase in emissivity for the processed surfaces. The base aluminum is pure metal, and the surface oxide is a dielectric. The thickness of the oxide layer varies greatly depending on the processing parameters.

Theoretical evaluation of total hemispherical emissivity of a surface. In order to provide the appropriate theoretical background on the different emissivity notations, a mathematical representation is included here. A diagram showing the measurement setup is illustrated in Supplementary Fig. S1. The spectral directional emissivity, $\varepsilon(\theta, \varphi, \lambda, T)$, of an opaque material is obtained in accordance with Kirchhoff's Law of thermal equilibrium shown in Supplementary Eq. 1:[2]

$$\varepsilon(\theta,\varphi,\lambda,T) = \alpha(\theta,\varphi,\lambda,T) = 1 - \rho(\theta,\varphi,\lambda,T), \quad (1)$$

where α and ρ are the spectral directional absorptivity and reflectivity, respectively. Most methods for calculating the emissivity of a surface are derived from these equations by computing the reflectance and

assuming no dependence on the solid angle φ, which means the spectral directional emissivity is assumed to be independent of the sample rotation. The spectral hemispherical emissivity, ε(λ, T), can be calculated from the spectral directional emissivity by using the following formula:[2]

$$\varepsilon(\lambda,T) = 2\int_0^{\pi/2} \varepsilon(\theta,\lambda,T)\sin\theta\cos\theta\,d\theta. \quad (2)$$

The total hemispherical emissivity, ε(T), is obtained via integration over the Planck distribution (P):[2]

$$\varepsilon(T) = \frac{\int_0^{\infty} \varepsilon(\lambda,T)P(\lambda,T)\,d\lambda}{\int_0^{\infty} P(\lambda,T)\,d\lambda}. \quad (3)$$

P is given by Supplementary Eq. 4:

$$P(\lambda,T) = \frac{8\pi hc}{\lambda^5 e^{\frac{hc}{\lambda kT}} - 1}, \quad (4)$$

where h is Planck's constant, k is the Boltzmann constant, c is the speed of light in vacuum, λ is the wavelength, and T is the temperature. It is important to note that the integral in Supplementary Eq. 3 is evaluated from 0 to infinity. However, experimentally it is not possible to make measurements that cover all wavelengths and, therefore, a finite wavelength range must be used. In Supplementary Eq. 3, the limits of integration correspond to the range of measurement (7.5- 14 μm).

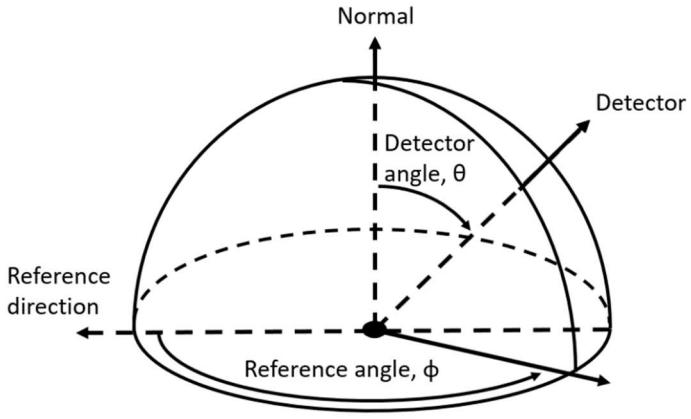

Supplementary Fig. S1 Depiction of emissivity measurement setup. In our case, the origin represents the sample and the detector is the thermal imaging camera. Samples were tested to verify no dependence of emissivity on the reference angle.

Measuring directional and hemispherical emissivity. In this work, the hemispherical emissivity is calculated from the experimentally measured directional emissivity by using conservation of energy and the Stefan-Boltzmann law (Supplementary Eqs. 5 and 6). Utilizing the measured temperature of the calibrated source and its emissivity, the temperature and thus the energy of the detector can be found. From here, the directional emissivity of the unknown sample can be calculated as a ratio of the temperature of the sample to that of the detector minus some small background contribution[7] (see Supplementary Eq. 5). The energies (E) of the detector, sample, and background are calculated from their temperatures by using the Stefan-Boltzmann law (see Supplementary Eq. 6):

$$E_{\text{detector}} = \varepsilon E_{\text{Sample}} + (1 - \varepsilon)\, E_{\text{background}}, \tag{5}$$

$$E = \sigma T^4. \tag{6}$$

Testing was performed to show that the sample reference direction (φ) had no effect on the emissivity (see Supplementary Fig. S1 for a depiction of the emissivity measurement setup). The hemispherical emissivity, ε_h, is calculated by using Supplementary Eq. 7. Note that the only difference between Supplementary Eqs. 7 and 2, the equation for calculating the spectral hemispherical emissivity, is the lack of a spectral dependence in Supplementary Eq. 7.

$$\varepsilon_h = \varepsilon(\mathrm{T}) = 2\int_0^{\pi/2} \varepsilon(\theta,\mathrm{T}) \sin\theta \cos\theta \, \mathrm{d}\theta \tag{7}$$

However, experimentally we make measurements at discrete angles (not as a continuous function) and the integral described in Supplementary Eq. 7 must be approximated. For the approximation we employ two methods, the rectangular[8] and trapezoidal integration approximation, and use the average between them. The rectangular approximation tends to overestimate the area of a concave down curve and underestimate concave up, whereas the trapezoidal approximation has the opposite effect. The difference in these two estimations is used to find the geometric uncertainty in the hemispherical emissivity.

Verifying our method for measuring emissivity. Two approaches were used to verify the validity of the presented technique for measuring emissivity. First, the hemispherical emissivity of three pieces of mirror- polished aluminum 6061 with an average surface roughness of less than 0.5 μm was measured three times and averaged. The resulting experimental values are reported in Supplementary Fig. S2. They are typical of mirror polished aluminum and found to be in good agreement with experimental results from the literature ranging between 0.04 to 0.09[2,3,5,6]. Simulation results for the emissivity of a flat aluminum surface as well as analytical values calculated using the equations in Ref.[2] are also included in Supplementary Fig. S2. The 23% difference in hemispherical emissivity between the experimental and theoretical values is likely a result of the native oxide layer formed on all aluminum surfaces, as well as the surface roughness. Both these effects are not included in this theoretical modeling.

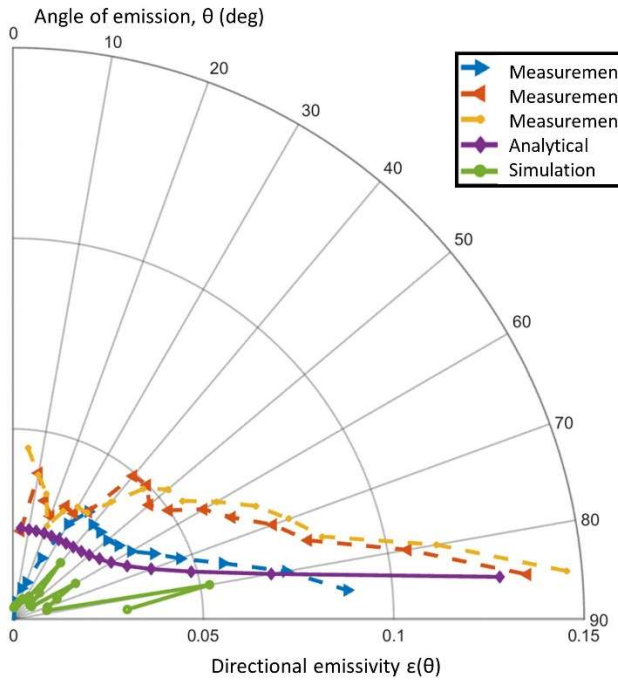

b

Hemispherical emissivity of bare flat aluminum	
Experimental	
Measurement 1	0.0462 +/-0.0014
Measurement 2	0.0600 +/-0.0018
Measurement 3	0.0582 +/-0.0017
Average	0.0548 +/-0.0016
Theoretical	
Analytical	0.0445
Simulation	0.0414

Supplementary Fig. S2 Experimental and theoretical values for hemispherical emissivity of bare flat aluminum. (**a**) Plot of experimental directional emissivity of bare aluminum measured using the thermal camera method as compared to theoretical values. The analytical and simulated data does not account for the surface roughness of the bare aluminum. (**b**) Table containing experimental hemispherical emissivity compared to the analytical and simulated values. The analytical value was calculated using the equations in Ref.[2].

The calibrated source used was a single roll of black polyvinyl chloride electrical tape. The reflection-based instrument (Surface Optics ET-100) was used to measure its hemispherical emissivity and directional emissivity at 20 and 60 degrees. These three values were used to fit a curve made by taking the average of 40 measurements of the tape's temperature in increments of five-degree angles to compute the absolute emissivity values. Because the sample is in thermal equilibrium, the apparent change in temperature measured by the thermal camera for different angles is actually a change in emissivity (see Supplementary Eqs. 5 and 6). Fitting the temperature measurements from the thermal camera to the emissivity measurements with the ET-100 results in the directional emissivity curve for the tape illustrated in Supplementary Fig. S3.

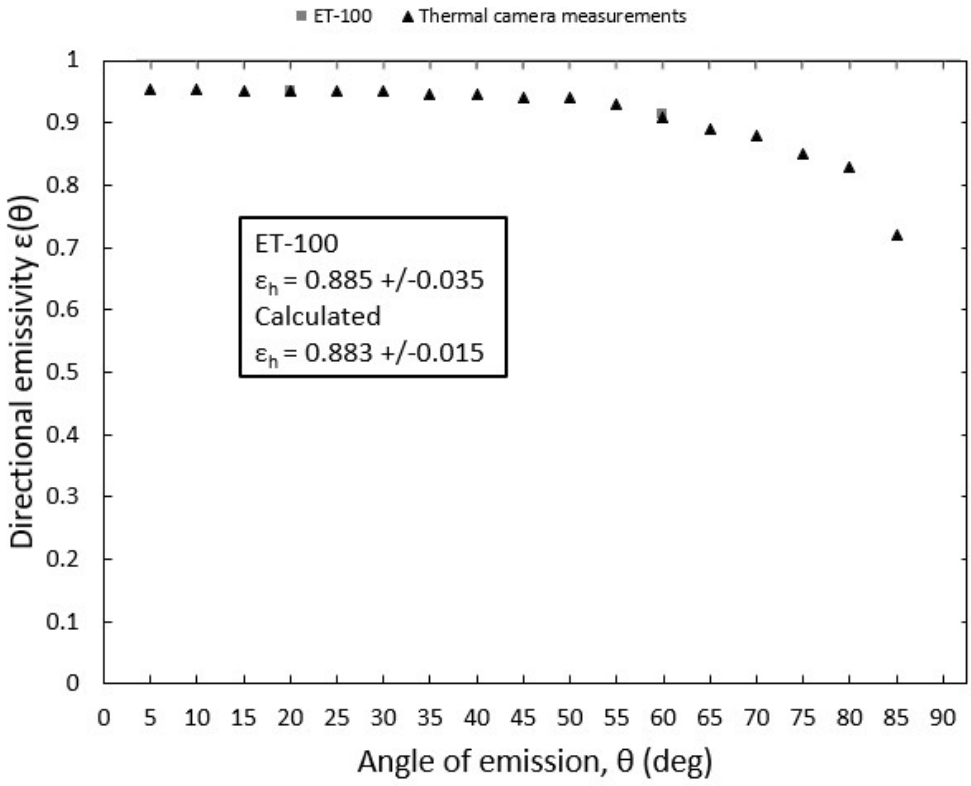

Supplementary Fig. S3 Directional and hemispherical emissivity of the black polyvinyl chloride electrical tape used as the calibrated source.

In addition, the emissivity of the best performing sample (described in the Results section (see Fig. 1)) was measured using a reflection-based instrument (Surface Optics SOC-100), which provides the reflection coefficient as a function of wavelength. The results were compared with our thermal imaging camera (TIC) testing method and are illustrated in Fig. S4. The difference between the measured hemispherical emissivity for the two techniques is negligible and less than 0.5%.

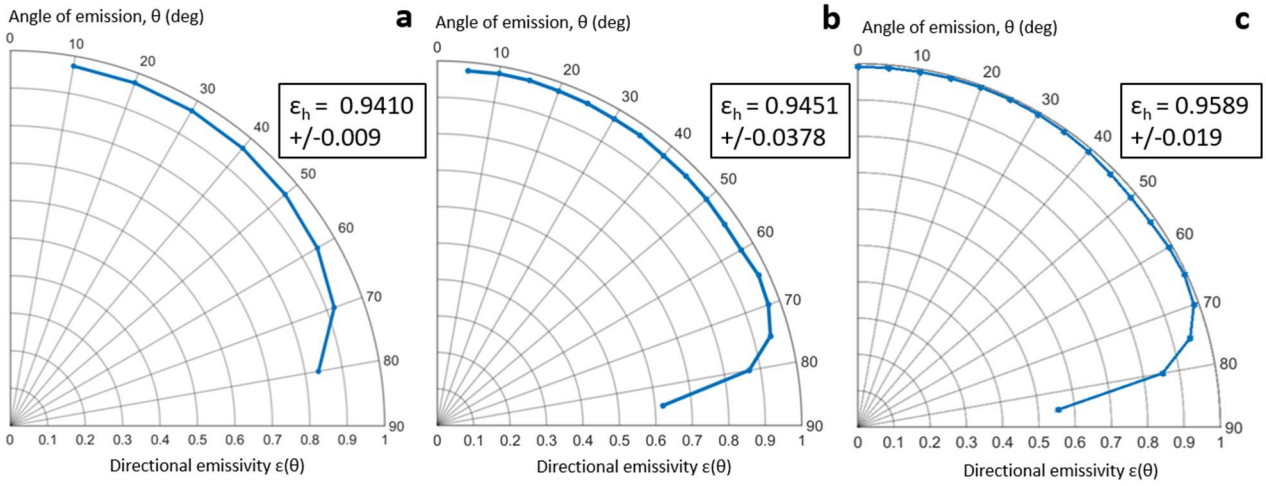

Supplementary Fig. S4 Directional and hemispherical emissivity of the best performing surface. This surface is shown in Fig. 1 in the main paper. Measurements made using the (**a**) reflection method, (**b**) TIC method, and (**c**) simulations. All three methods are described in more detail in the Supplementary Information section and they are in agreement within the uncertainty values.

Supplementary Discussion 2

Extended measurement data. As noted in the Results section, directional and hemispherical emissivity measurements and SEM images for additional surfaces processed with varied fluence and processed either in nitrogen or in air are included in Supplementary Figs. S5 and S6, respectively. The cross section in Supplementary Fig. S7 is included as an example to demonstrate how, at relatively high fluence values, the oxidized nanoparticles redeposit in a non-uniform manner resulting in the emissivity drop that occurs with increased fluence beyond 3 J cm^{-2}. Energy Dispersive X-Ray Spectroscopy (EDS) surface area scans for both atmospheres are included in Supplementary Fig S8 to demonstrate the dramatic difference in surface composition between the two environments. Based on the EDS surface scans, processing in nitrogen appears to result in reduced oxygen content compared to processing in air. Supplementary Figures S9 and S10 include one EDS line scan for each of the cross sections presented in Figs. 2 and 3 in the main paper. This line scan data is included to demonstrate the chemical analysis performed to determine the composition of the layers formed during processing.

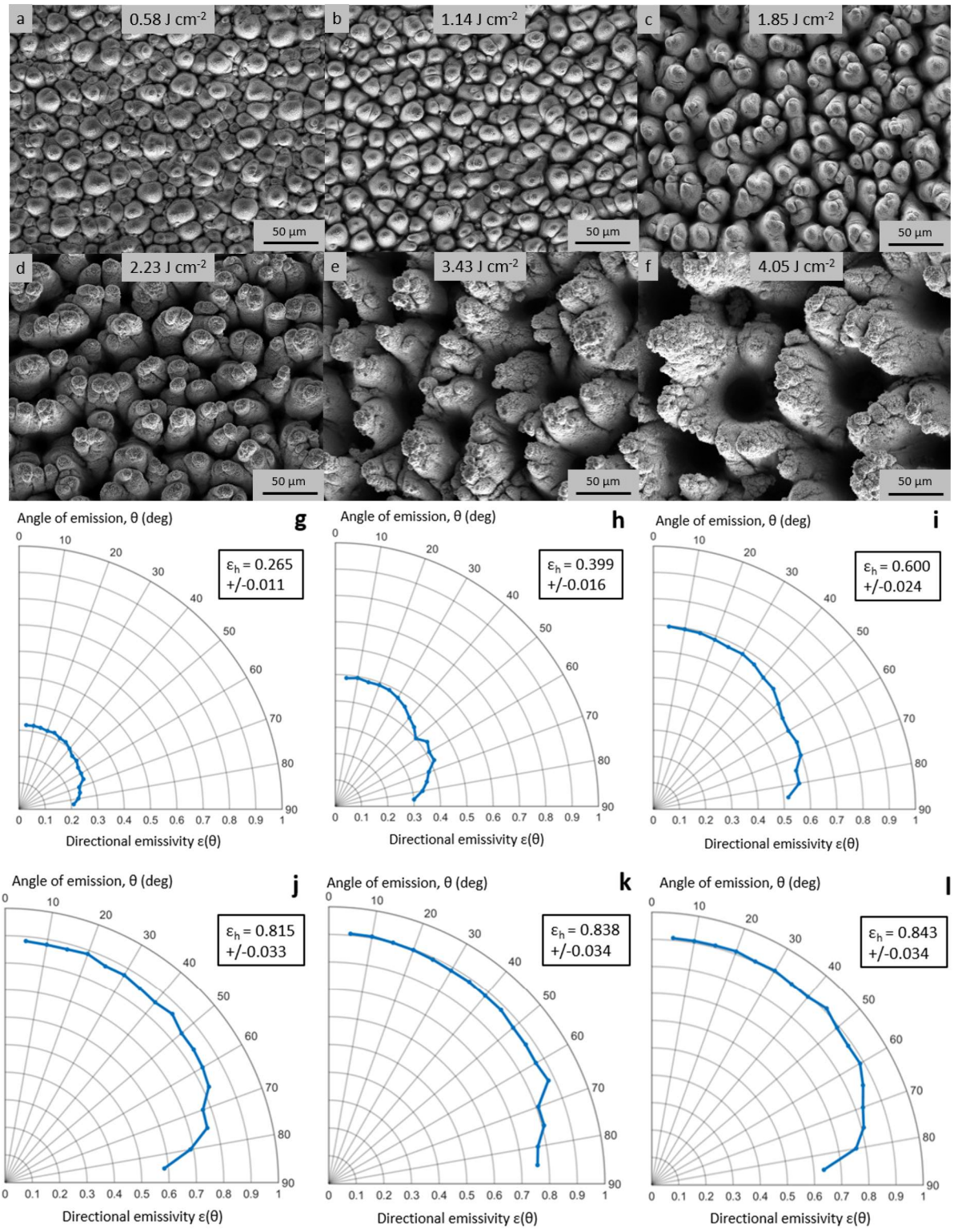

Supplementary Fig. S5 SEM images, as well as directional and hemispherical emissivity of surfaces processed in nitrogen. (**a**-**f**) SEM images of samples produced at different fluences for a constant pulse count of 1865. (**g**-**l**) The directional and hemispherical emissivity of the samples. The SEM image in (**a**) corresponds to the emissivity plot in (**g**), (**b**) corresponds to (**h**), and so on.

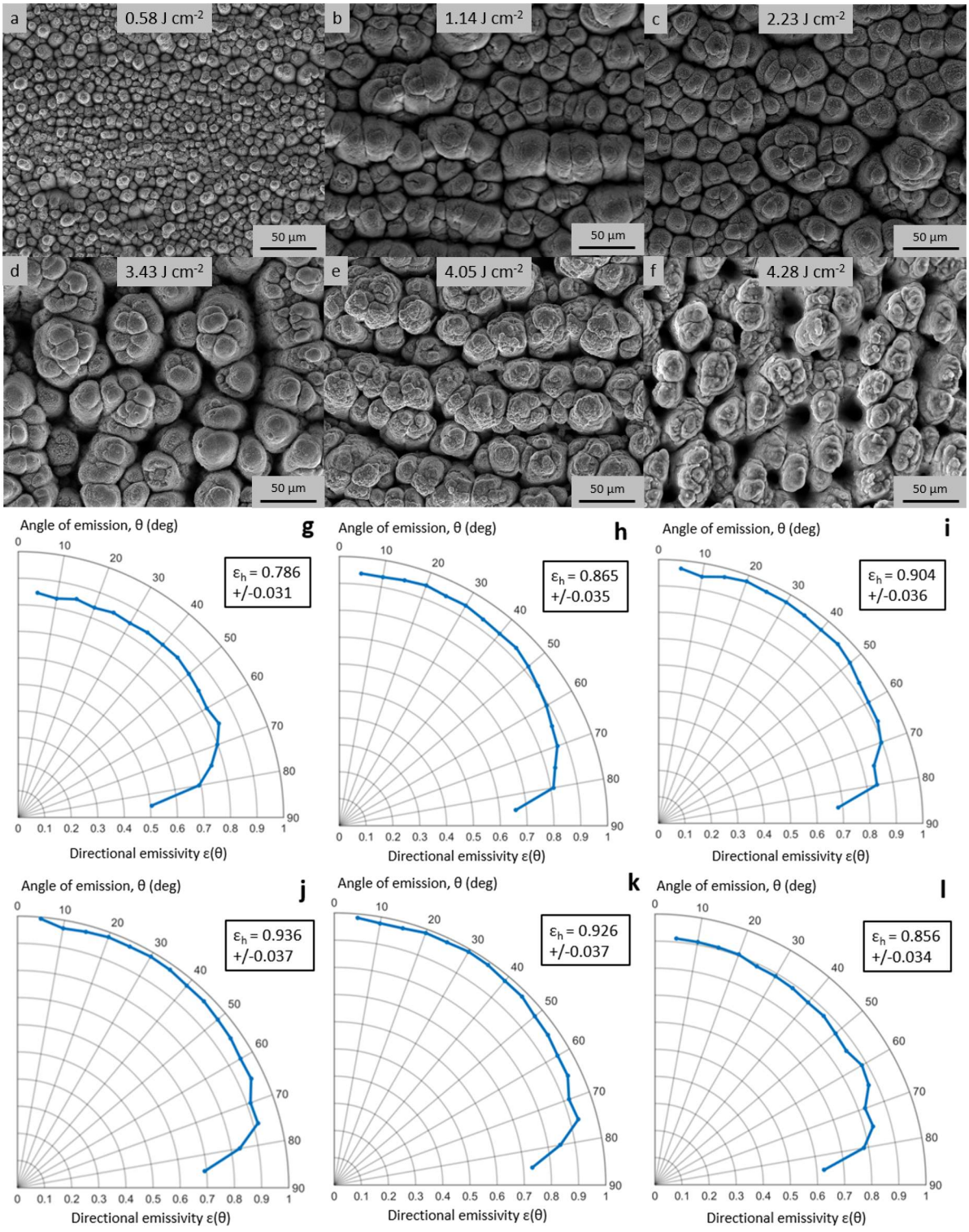

Supplementary Fig. S6 SEM images, as well as directional and hemispherical emissivity of surfaces processed in air. (**a**-**f**) SEM images of samples produced in air at different fluences for a constant pulse count of 1865. (**g**-**l**) The directional and hemispherical emissivity of the samples. The SEM image in (**a**) corresponds to the emissivity in (**g**), (**b**) corresponds to (**h**), and so on.

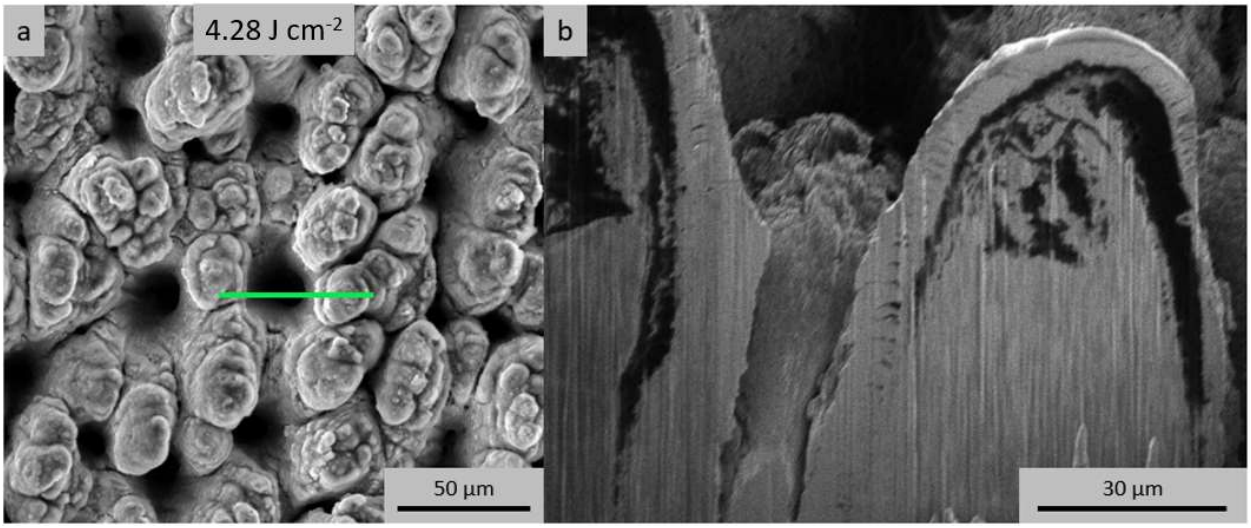

Supplementary Fig. S7 Surface and subsurface images for a sample produced in an air environment to show the decrease in thickness of the oxide layer moving down into the pit. (**a**) Surface SEM image of a sample produced at the fluence specified in the grey box in the top middle of the image for a constant pulse count of 1865. (**b**) Ion beam image of the area through a pit between two mounds (green line in (**a**)) that was cross sectioned with the FIB mill to show the subsurface structure.

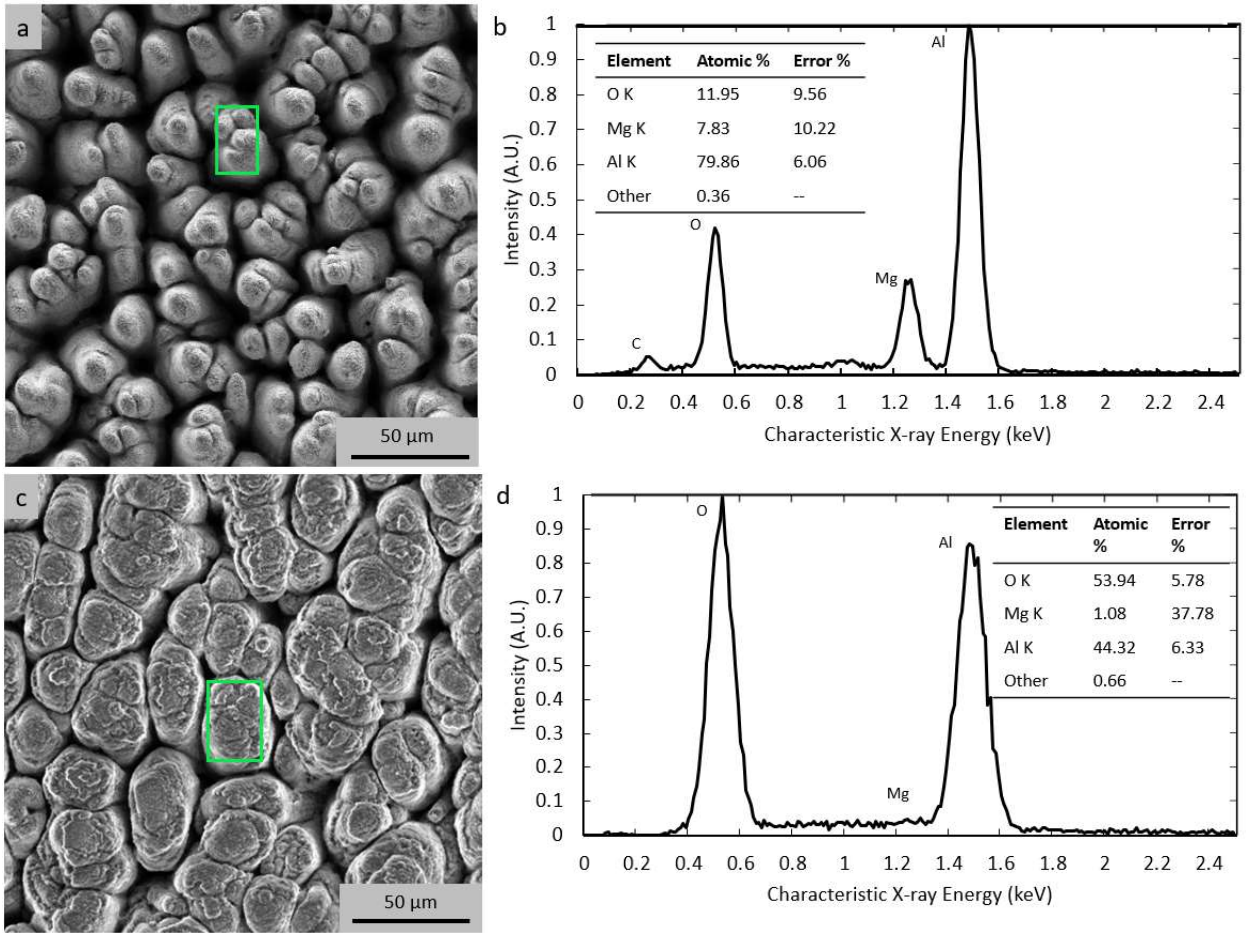

Supplementary Fig. S8 EDS surface scans for samples produced in each environment. The area scan EDS data on the right was collected over the area within the green boxes in the SEM images on the left. (**a, b**) Results for a sample processed in nitrogen at a fluence of 1.85 J cm^{-2} and a pulse count of 1865 with an oxide layer less than 0.5 µm thick. (**c, d**) Results for a sample processed in air at a fluence of 2.86 J cm^{-2} and a pulse count of 1865 with an oxide layer of 6.5+/-2.5 µm thick. The lower magnesium content for the sample processed in air (**c, d**) is likely because signal is only being collected from the thick oxide layer. For the samples processed in nitrogen (**a, b**) the oxide is less than 500 nm thick, so some signal is collected from the bulk Al 6061 material, which contains Mg as an alloying element. The EDS results are indistinguishable between samples produced in the same environment.

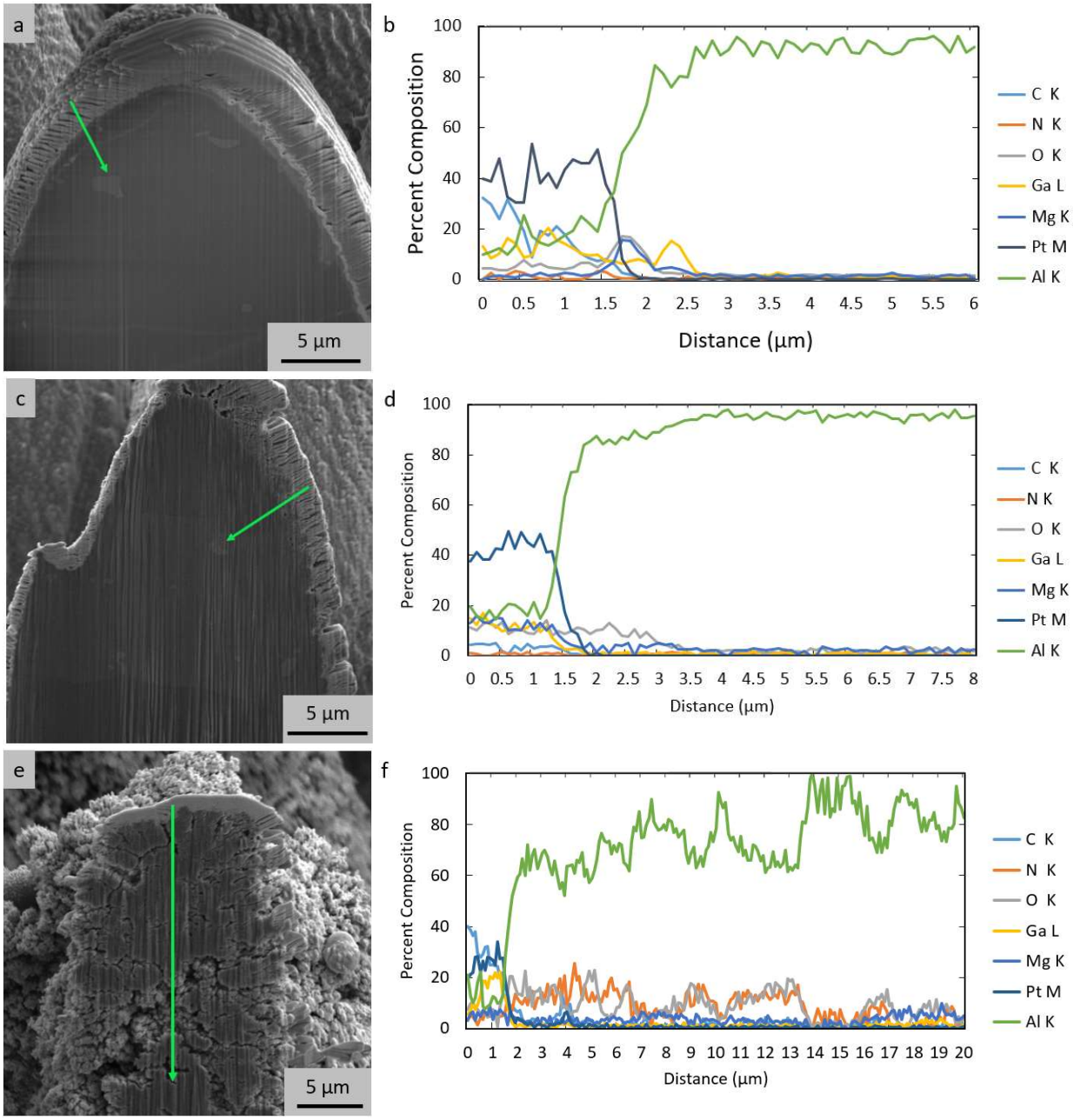

Supplementary Fig. S9 EDS line scans for samples produced in a nitrogen environment. The cross-sectional SEM images on the left correspond with Fig. 2 in the main paper. The green arrows in the SEM images on the left indicate the scan path that corresponds with the EDS line scan data on the right. The samples were processed with a fluence of 0.58 J cm^{-2} (**a-b**), 1.85 J cm^{-2} (**c-d**), and 4.05 J cm^{-2} (**e-f**), and a pulse count of 1865. The alternating bands of relatively high aluminum versus oxygen seen in (**e-f**) are caused by the porosity.

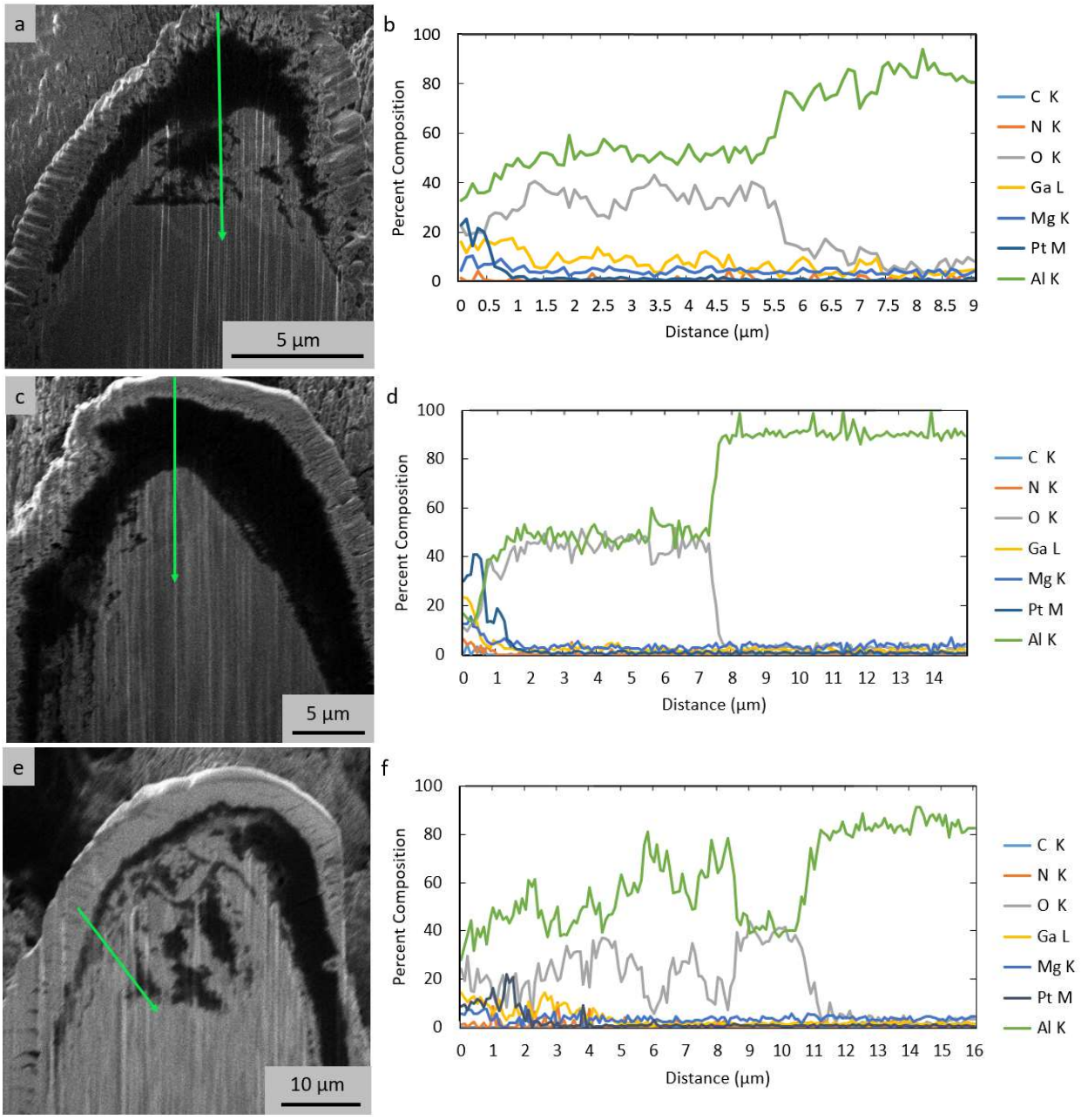

Supplementary Fig. S10 EDS line scans for samples produced in an air environment. The cross-sectional SEM images on the left correspond with Fig. 3 in the main paper. The green arrows in the SEM images on the left indicate the scan path that corresponds with the EDS line scan data on the right. The samples were processed with a fluence of 0.58 J cm^{-2} (**a-b**), 2.86 J cm^{-2} (**c-d**), and 4.28 J cm^{-2} (**e-f**), and a pulse count of 1865.

Supplementary Discussion 3

Theoretical simulations of a flat aluminum surface. Simulations of an ideal polished flat aluminum surface can be found in Supplementary Fig. S2 and agree with experimental and analytical results found in the relevant literature[2–6,9–13]. The emissivity of aluminum with an oxide layer on top was also simulated to further verify the theoretical model. Polished aluminum can be anodized to grow a thick oxide layer on its surface. Experimental data shows that the hemispherical emissivity of the aluminum/aluminum-oxide system increases rapidly until the oxide thickness of about 15 μm, where it levels out, asymptotically approaching ~0.85 for larger oxide thicknesses[11–13]. Simulations, illustrated in Supplementary Fig. S11, were performed for 5, 15, and 20 μm oxide layer thickness and agree with the experimental data reported in the literature.

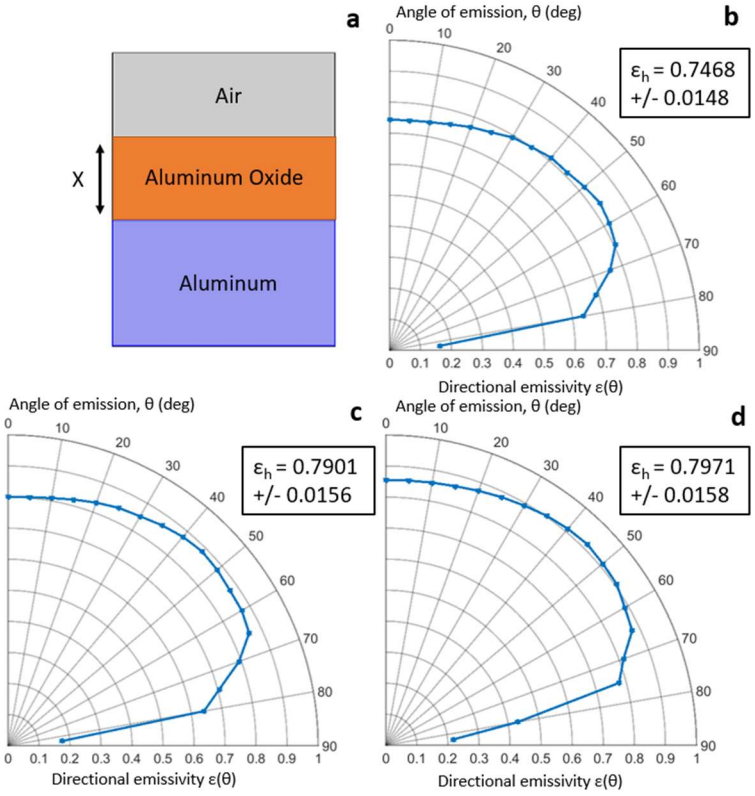

Supplementary Fig. S11 Theoretical simulations of hemispherical and directional emissivity for a flat thick aluminum film with varying thickness of top oxide. (**a**) The schematic of the system used in the simulations. Simulation results for an oxide layer thicknesses of (**b**) 5 μm, (**c**) 15 μm, and (**d**) 20 μm.

Theoretical study of different structural morphologies effects on the emissivity. In this section we present a comprehensive theoretical study to provide additional physical insights on the influence mechanism of the structure on the emissivity properties of different FLSP surfaces. Towards this goal, we perform full-wave rigorous electromagnetic simulations (similar to Fig. 5 in the main paper) to accurately demonstrate the effects of diverse structural morphologies on the emissivity of different FLSP surfaces. More specifically, we study the emissivity dependence to both the thickness of aluminum oxide, as well as the number of mounds with different sizes produced via the FLSP process. The dimensions of the simulated FLSP structures follow the sizes of the mounds in the experimental cross-sectional images shown in the main paper. The emissivity is again computed in the mid-IR range and its average value is plotted as a function of different emission angles, similar to Fig. 5 and the other experimental results presented in the main paper.

We start our theoretical studies by simulating a single aluminum mound surrounded by periodic boundary conditions at the left and right sides. This consists a simplified unit cell of the usually complex FLSP surface morphology (Fig. 1b in main paper). The computed directional emissivity results with increasing aluminum oxide thickness are shown in Supplementary Fig. S12. In all these simulations, we keep the diameter of the hemispherical aluminum mound to the fixed value of 30 μm. Interestingly, the emissivity is very limited and low in the case for a bare aluminum mound with no oxide formed on top, as shown in Supplementary Fig. S12a. As the thickness of the aluminum oxide layer increases, the directional emission is also enhanced, which is evident by the remaining plots in Supplementary Fig. S12. From these results, it can be concluded that for oxide layer thicknesses larger than 5 μm the emissivity is almost perfect, at least until emission angles of 70 degrees. This response is consistent with the experimental results shown in the main paper.

Next, we compute the emissivity of a supercell, similar to Fig. 5e in the main paper, but now composed of two and three hemispherical mounds with different dimensions and with varied oxide layer thicknesses. The relevant directional emissivity results along with the simulation schematics are shown in

Supplementary Figs. S13. and S14, respectively. Again, we keep the diameters of the hemispherical aluminum mounds fixed in all simulation models and equal to a_1 = 30 μm, a_2 = 20 μm, and a_3 = 10 μm. To ensure the same rate of oxide growth on top of each aluminum mound, the thickness of each oxide layer is changed proportionally to the oxide thickness added on the first mound, d_1, by using the relations: $d_2 = a_2 \cdot d_1 / a_1$ and $d_3 = a_3 \cdot d_1 / a_1$. Directional emissivity enhancement is obtained by increasing the thickness of aluminum oxide on top of the different morphologies of aluminum mounds, as is evident by Supplementary Figs. S13 and S14. However, in these supercell cases, the emissivity is almost perfect for emission angles even higher than 70 degrees, on the contrary to the single mound design shown in Supplementary Fig. S12. This is the main reason that a supercell was used in the simulations of the main paper (Fig. 5) instead of a single mound. Hence, it can be concluded that the supercell geometry (either two or three mounds) follows more accurately the morphology and dimensions of the experimentally obtained quasiperiodic FLSP surfaces.

Finally, it is worthwhile to mention that perfect emissivity from the FLSP surfaces is only due to the micrometer-scale geometrical features and the oxide layer and is not related to the nanoscale features. We checked this issue by modelling the single mound geometry at the nanometer scale with nanoscale dimensions (a_1 = 30 nm and d_1 = 15 nm) and concluded that the emissivity is very low, as shown in Supplementary Fig. S15. The nanometer-scale geometrical features of the FLSP surfaces do not play a role in the computed mid-IR emissivity since the wavelength range of this mid-IR response is in the tens of micrometer scale (7.5 to 14 μm), which is tens to thousands of times larger than the nanometer scale morphological features.

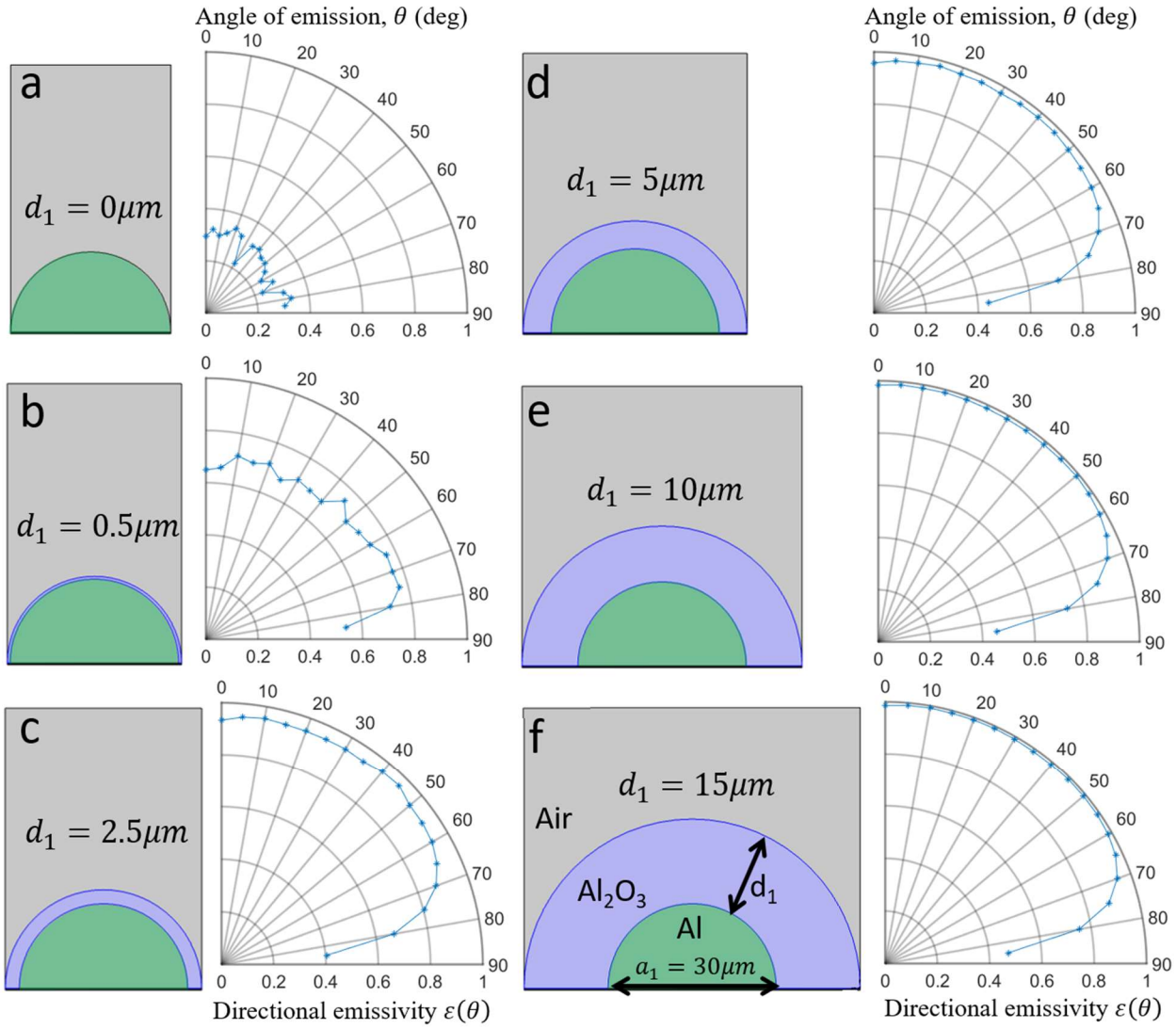

Supplementary Fig. S12 The emissivity of a single periodic aluminum mound with varying aluminum oxide thicknesses. (**a-f**) Schematic geometries and corresponding computed directional emissivity values of a single periodic aluminum mound with varying aluminum oxide thicknesses ranging from 0 μm in (**a**) (bare aluminum mound) to 15 μm in (**f**). The aluminum mound has a fixed diameter of 30 μm.

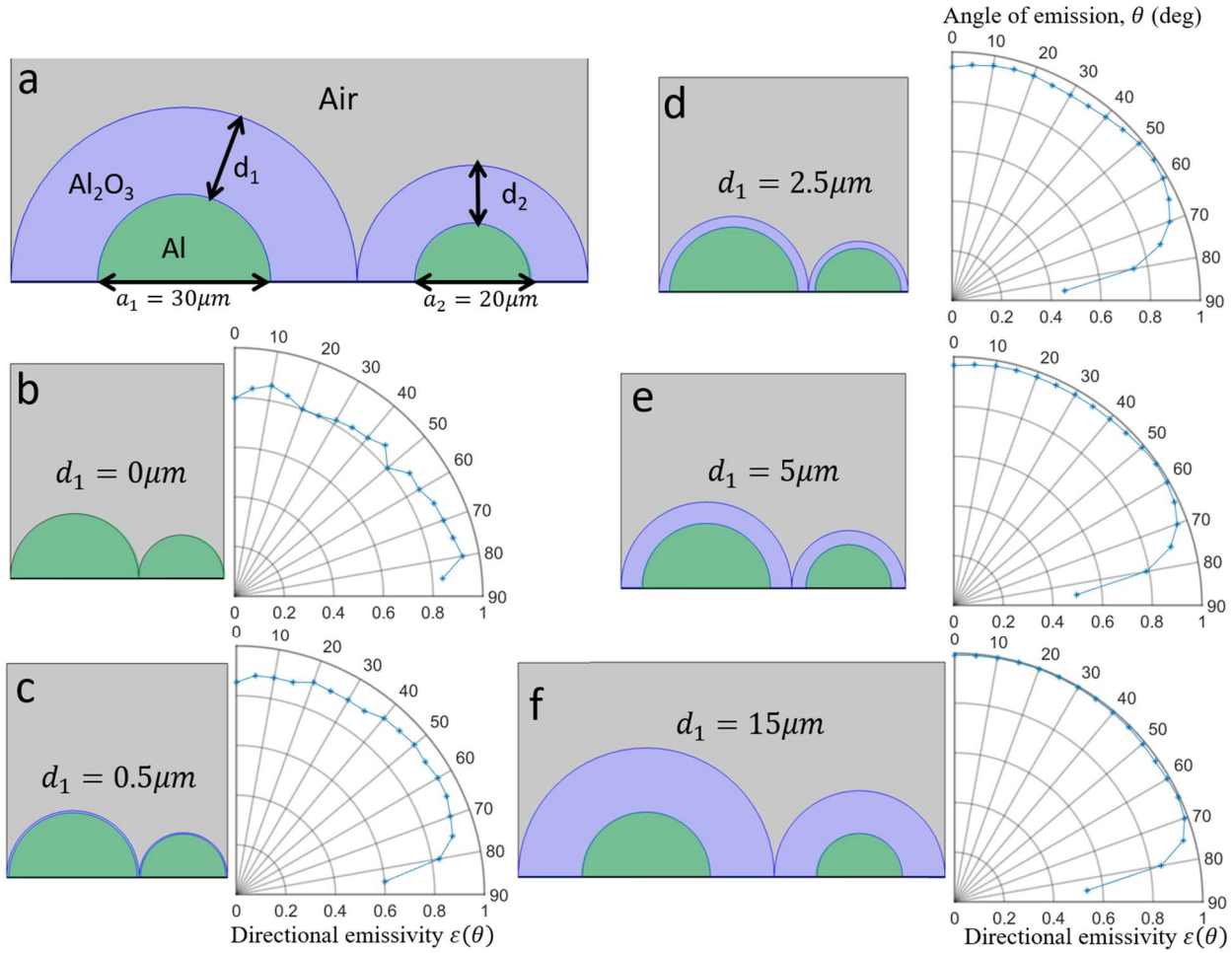

Supplementary Fig. S13 The emissivity of two periodic aluminum mounds with varying aluminum oxide thicknesses. (**a**) Schematic of two periodic aluminum mounds with varying aluminum oxide thicknesses. The aluminum mounds have fixed diameters of a_1 = 30 μm and a_2 = 20 μm, respectively. (**b-f**) Schematic geometries and corresponding computed directional emissivity values. The thicknesses of the aluminum oxide layer ranging from d_1 = 0 μm in (**b**) to d_1 = 15 μm in (**f**). The thickness of the second mound aluminum oxide layer d_2 changes proportionally to the thickness of the first oxide layer d_1 by using the relation: $d_2 = a_2 \cdot d_1 / a_1$.

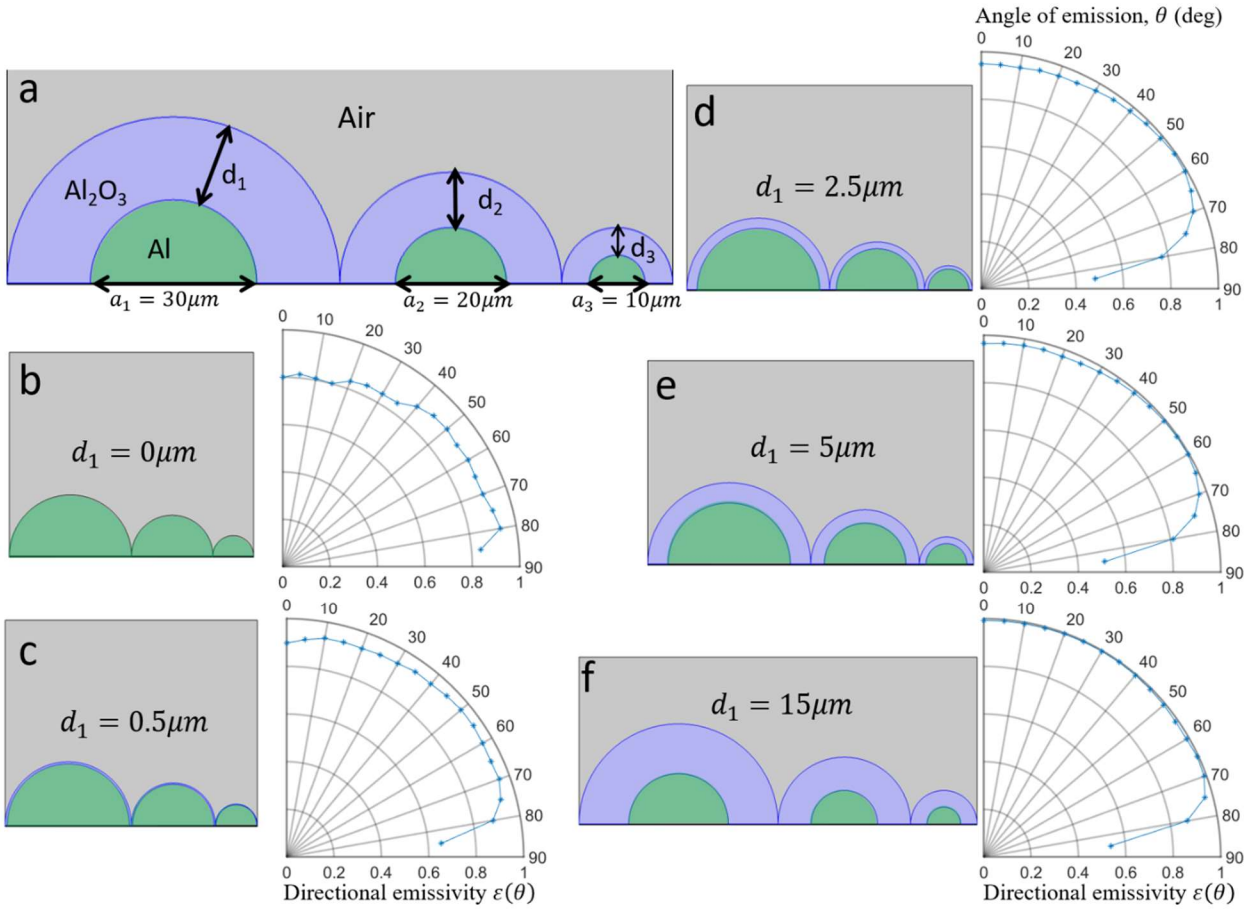

Supplementary Fig. S14 The emissivity of three periodic aluminum mounds with varying aluminum oxide thicknesses. (**a**) Schematic of periodic three aluminum mounds with varying aluminum oxide thicknesses. The aluminum mounds have fixed diameters of a_1 = 30 μm, a_2 = 20 μm, and a_3 = 10 μm, respectively. (**b-f**) Schematic geometries and corresponding computed directional emissivity values. The thicknesses of aluminum oxide layer ranging from d_1 = 0 μm in (**b**) to d_1 = 15 μm in (**f**). The thicknesses of the second and third mound aluminum oxide layers d_2 and d_3, respectively, change proportionally to the thickness of the first oxide layer d_1 by using the relations: $d_2 = a_2 \cdot d_1 / a_1$ and $d_3 = a_3 \cdot d_1 / a_1$.

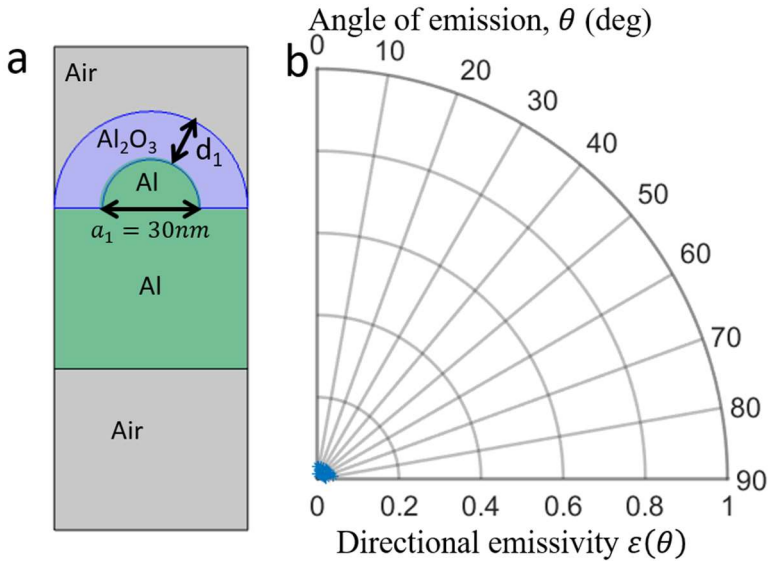

Supplementary Fig. S15 The resulted mid-IR emissivity is extremely low for nanoscale mound morphologies. (**a**) Schematic of a single periodic aluminum mound with nanoscale dimensions (a_1 = 30 nm and d_1 = 15 nm). (**b**) Computed directional emissivity values. Note the directional emissivity for Supplementary Fig. S2 is plotted from 0 to 0.15 but is plotted from 0 to 1 here.

Supplementary Discussion 4

Statistical information. The uncertainty in hemispherical emissivity values measured using the thermal imaging camera (TIC) based technique described in the Supplementary Discussion 1 is accounted to two causes. First, for most samples, because the directional emissivity is consistent across all angles with only a slight decrease after 65 degrees, the geometric error caused by approximating the value of the integral to calculate hemispherical emissivity from the directional measurements is less than 2%. The remaining uncertainty is accounted for in the 2% error from the thermal camera, as stated by the manufacturer. The reflection-based instrument (Surface Optics SOC-100) has an uncertainty of 1% overall for hemispherical and directional emissivity measurements, as quoted by the manufacturer. The maximum hemispherical emissivity value reported is the average of 24 measurements, two per each of the 12 samples produced in six batches using two laser systems at three different times. The standard deviation of the 24 measurements is also reported.

The reported measured surface roughness parameters are the average and standard deviation from the LSCM scans. For the background gas experiment, three LSCM scans from different locations on each sample were used. For the acid etching experiment, four LSCM scans were used, two scans per sample at each given etching parameter. For each scanned area, the average roughness (R_a) was measured over the entire scanned area. The average height was the average of the maximum height (R_z) measurement for ten subset areas within each scanned area.

Supplementary References

1. Wen, C. Da & Mudawar, I. Modeling the effects of surface roughness on the emissivity of aluminum alloys. *Int. J. Heat Mass Transf.* **49**, 4279–4289 (2006).

2. Siegel, R. & Howell, J. R. *Thermal Radiation Heat Transfer*. (Taylor and Francis Group, 1992).

3. Wen, C. Da & Mudawar, I. Modeling the effects of surface roughness on the emissivity of aluminum alloys. *Int. J. Heat Mass Transf.* **49**, 4279–4289 (2006).

4. Wen, C. & Mudawar, I. Experimental Investigation of Emissivity of Aluminum Alloys and Temperature Determination Using. *J. Mater. Eng. Perform.* **11**, 551–562 (2002).

5. Bartl, J. & Baranek, M. Emissivity of aluminium and its importance for radiometric measurement. *Meas. Sci. Rev.* **4**, 31–36 (2004).

6. Sully, A. H., Brandes, E. A. & Waterhouse, R. B. Some measurements of the total emissivity of metals and pure refractory oxides and the variation of emissivity with temperature. *Br. J. Appl. Phys.* **3**, 97–101 (1952).

7. Denmead, O.T., Raupach M.R., Leuning R., Dunin F.X., F. J. R. Micrometeorology in Agricultural Systems. in *Micrometeorology in agricultural systems* (ed. Hatfield J.L. and Baker J.M.) 485–511 (American Society of Agronomy, 2005).

8. King, J. L., Jo, H., Loyalka, S. K., Tompson, R. V. & Sridharan, K. Computation of total hemispherical emissivty from directional spectral models. *Int. J. Heat Mass Transf.* **109**, 894–906 (2017).

9. Palik, E. D. *Handbook of optical constants of solids*. *Handbook of Optical Constants of Solids* vol. 1 (Academic Press, 1985).

10. Kischkat, J. *et al.* Mid-infrared optical properties of thin films of aluminum oxide, titanium

dioxide, silicon dioxide, aluminum nitride, and silicon nitride. *Appl. Opt.* **51**, 6789–6798 (2012).

11. Brannon, R. R. & Goldstein, R. J. Emittance of Oxide Layers on a Metal Substrate. *ASME-Paper 69-WA/HT-4* 257–263 (1969).

12. Hass, G. On the Preparation of Hard Oxide Films with Precisely Controlled Thickness on Evaporated Aluminum Mirrors*. *J. Opt. Soc. Am.* **39**, 532 (1949).

13. Thomas, J. K. & Ondrejcin, R. S. An evaluation of the thickness and emittance of aluminum oxide films formed in low-temperature water. *J. Nucl. Mater.* **199**, 192–213 (1993).